Nonlinear Görtler Vortices and Their Secondary Instability in a Hypersonic Boundary Layer

Fei Li* and Meelan Choudhari†
NASA Langley Research Center, Hampton, VA, 23681

Pedro Paredes‡
National Institute of Aerospace, Hampton, VA, 23666

Nonlinear development of the Görtler instability over a concave surface gives rise to a highly distorted inflectional flow field in the boundary layer that leads to both wall-normal and spanwise gradients in the flow. Such nonlinear structures are susceptible to strong, high-frequency secondary instabilities that may lead to the onset of laminar-turbulent transition. The present numerical study uses direct numerical simulations and linear secondary instability theory to investigate finite amplitude Görtler vortices and their secondary instability characteristics, respectively, in the hypersonic flow over an axisymmetric cone with a concave aft body. To complement previous studies in the literature wherein the Görtler instability was usually studied for a flat plate and initiated at some upstream location by imposing an eigenfunction as the inflow condition or by blowing and suction at the wall, the present investigation is focused on fully realizable Görtler instability that is excited by an azimuthally periodic array of surface protuberances. Furthermore, while the previous work had mostly focused on the secondary instability of Görtler vortices with cross-plane velocity contours that resembled bell-shaped structures, the present results confirm that fully developed mushroom structures also exist in the hypersonic regime when the Görtler vortex amplitude is sufficiently large. Computations further reveal that the dominant modes of secondary instability in these mushroom-shaped structures correspond to an antisymmetic (i.e., sinuous) "stem" mode that concentrates within the strong, nearly wall-normal internal shear layers surrounding the stem regions underneath the caps of the mushroom structures. Additionally, there exist a multitude of other significantly unstable secondary instability modes of both symmetric and antisymmetric types. Analogous to the secondary instability of crossflow vortices in hypersonic flows, secondary instability modes originating from the Mack mode instability play an important role during the nonlinear breakdown process.

Nomenclature

A_u = local amplitude of Görtler vortex [m/s]
$A_{u\,ref}$ = reference amplitude of Görtler vortex [m/s] at X = 0.32 m
G = Görtler number, $(U_e\theta/\nu)(\theta/R)^{1/2}$
h = roughness height [mm]
h_{ref} = reference roughness height = 0.005 mm
M_e = boundary-layer edge Mach number
M_∞ = freestream Mach number
N = logarithmic amplification ratio
P_∞ = freestream pressure [Pa]
R = surface radius of curvature in streamwise direction
Re_∞ = freestream unit Reynolds number [m^{-1}]
T = temperature [K]
T_w = wall temperature [K]
T_∞ = freestream temperature [K]
U = streamwise velocity [m/s]
U_e = boundary-layer edge velocity [m/s]
X = axial coordinate [m]
Y = wall-normal distance [m]
$\delta_{0.995}$ = boundary-layer thickness corresponding to 0.995 times total enthalpy in free stream [mm]
δ^* = boundary-layer displacement thickness [mm]
θ = boundary-layer momentum thickness [mm]

* Aerospace Technologist, Fei.Li@nasa.gov
† Aerospace Technologist, Meelan.M.Choudhari@nasa.gov, Fellow, AIAA.
‡ Research Engineer, pedro.paredes@nasa.gov, Senior Member, AIAA.

I. Introduction

Laminar boundary layers over concave surfaces are susceptible to Görtler instability that often appears in the form of stationary counterrotating streamwise vortex pairs [1-29]. The Görtler instability essentially represents a form of centrifugal instability that causes the stationary vortex structures to amplify along the flow direction. Finite amplitude Görtler vortices give rise to highly inflectional flow fields, and therefore, can themselves become unstable to high-frequency secondary instabilities after reaching a certain threshold amplitude [24-26]. The rapid growth of these secondary instabilities may initiate a breakdown of the laminar flow into turbulence. The Görtler instability can occur at all flow speeds, ranging from incompressible flow to hypersonic Mach numbers. However, their characteristics can vary significantly across this speed regime. Literature on the Görtler instability in incompressible, subsonic, and supersonic boundary layers is quite extensive and has been reviewed by Saric [27]. More recent works on the topic have also been discussed by Ren and Fu [25]. In the hypersonic regime, regions of concave streamline curvature may occur in several different applications, ranging from compression surfaces ahead of the combustor within a hypersonic scramjet engine to the nozzles in hypersonic wind tunnels. A typical nozzle contour includes a significant region of concave surface curvature, and therefore, the amplification of Görtler instability tends to play an important role during laminar-turbulent transition in the boundary layer flow along the nozzle wall [11, 15, 28]. Because of the intense acoustic radiation from transitional and turbulent boundary layers at hypersonic speeds, the onset of transition along the nozzle wall is accompanied by a significant increase in the intensity of the wind tunnel disturbance environment. For this reason, the control of transition via Görtler instability is of critical importance in the development of low disturbance, i.e., quiet hypersonic wind tunnels [11, 28].

Görtler vortices and the associated secondary instability in a hypersonic flow were studied by Li et al. [24] for the test section of the Boeing/AFOSR Mach 6 wind tunnel at Purdue University [28]. Amplification due to the Görtler mechanism was also an important part of roughness-induced tripping over the HyperX configuration[23]. For the range of Görtler vortex amplitudes examined by Li et al. [24], the computed flow field did not reveal any mushroom structures with a thin stem in the vicinity of the symmetry line, in spite of their ubiquitous presence among Görtler vortices in lower speed flows. Instead, the velocity contours within the distorted flow field were shaped like a bell. The secondary instability eigenfunctions of various modes were concentrated on the edge region of the bell. Subsequently, Ren and Fu [25] carried out a parametric study of Görtler instability and its associated secondary instability across a range of Mach numbers and spanwise wavenumbers. They also found that, at a hypersonic Mach number of 6, the flow field in the presence of Görtler vortices resembled the shape of a bell rather than a mushroom. In both studies, the secondary instability modes were found to be rather uninteresting at this Mach number, falling short of expectations that something new and dramatically different was going to be discovered. In retrospect, this may have been partly due to the reduced growth rates of the Görtler vortices in hypersonic speeds that prevented them from attaining sufficiently large amplitudes.

A recent collaborative effort between Purdue University and NASA focused on the technical risks associated with a potential application of distributed suction for the control of transition along the walls of a hypersonic nozzle [26]. To facilitate controlled wind tunnel measurements in an affordable manner, the above work focused on the external boundary layer flow over a suitably designed cone model, rather than the flow along the walls of a wind tunnel nozzle. The baseline design of the cone model had the requirement of supporting a sufficiently strong growth of Görtler instability for flow conditions of the abovementioned Mach 6 wind tunnel. Li et al. [26] studied several cone designs with a straight cone forebody and an aft body having a concave streamwise surface curvature. Again, they found that the distorted flow field associated with finite amplitude Görtler vortices had cross-plane velocity contours that resembled a bell shape, rather than the mushroom structure observed in lower speed flows supporting Görtler instability. One of the interesting findings of the secondary instability computations by Li et al. [26] was the existence of a symmetric unstable mode that originated from the Mack mode instability of the unperturbed boundary layer and was subsequently distorted by the presence of increasingly stronger modulation of the basic flow due to the axial growth of the Görtler vortices. The role of Mack modes in seeding certain mode(s) of the secondary instability was similar to that found earlier during both analysis and DNS of the secondary instability of crossflow vortices in a hypersonic boundary layer [29, 30].

As discussed above, a possible reason for the absence of the mushroom structure in the previous studies of Görtler instability in hypersonic flows may be related to the slower growth of the Görtler instability. Earlier DNS by Whang and Zhong [16] did find the mushroom structure at the very high Mach number of 15 and wall temperature of 1000K with perfect gas flow. However, they were unable to find any secondary instability growth for that case. Li et al. [24] and Ren and Fu [25] were able to find a limited number of unstable secondary stability modes even in the absence of the mushroom structure in the modified basic state produced by finite amplitude Görtler vortices. The subsequent study by Li et al.[26], which also focused on similar basic states, was able to uncover a few additional modes of secondary instability with significant amplification rates. Upon the completion of the present study, we came across the recently published work by Chen et al. [31], who report comprehensive computations of Görtler vortices and their secondary instability at Mach 6.5 by using DNS and temporal analysis of secondary instability theory. They were able to produce mushroom structures that support a large number of secondary instability modes, including the stem modes analyzed earlier by Ren and Fu [25] at low Mach numbers that were concentrated in the stem region of the mushroom structure. The secondary instability analysis by both Ren and Fu [25] and Chen et al. [31] is based on temporal eigenvalue problems, while Li et al. [24, 26] adopted the spatial approach that is more directly connected to the disturbance evolution over both wind-tunnel and flight configurations. Additionally, both Ren and Fu [25] and Chen et al. [31] used adiabatic thermal boundary condition at the model surface, while Li et al. [24, 26] analyzed the moderately cold-wall case with $T_w =$ 300 K that closely approximates the conditions of wind tunnel measurements in most short duration high-speed facilities.

The present study aims to produce Görtler vortices of sufficiently large amplitudes via a realizable disturbance source, in order to generate mushroom structures and analyze the associated secondary instability. The basic state computations of finite amplitude stationary Görtler vortices are described in Section II. Characteristics of the secondary instability sustained by those vortex structures are examined in Section III, whereas summary and concluding remarks based on this work are presented in Section IV.

II. Basic State Computation

Görtler instability in a boundary-layer flow manifests itself in the form of pairs of counter-rotating vortices aligned with the direction of the inviscid flow adjacent to the concave surface. When the vortex amplitude exceeds a certain threshold, the modified boundary layer flow becomes susceptible to more rapid growth of a three-dimensional, time dependent instability that is known as the secondary instability. In this section, we examine the evolution of the primary instability in the form of finite amplitude, stationary Görtler vortices for various initial amplitudes. The flow configuration of interest corresponds to an axisymmetric cone with a straight forebody and a concave aft body that was described in the previous study by Li et al. [26] (see Fig. 1, and details of the cone geometry are described in ref. [26]). Specifically, the linear stability analysis presented in the previous work showed that a particular configuration that was denoted as Configuration #9 in ref [26] was able to support a strong growth of stationary Görtler instability at the flow conditions of interest, which correspond to the nominally maximum quiet flow Reynolds number in the Boeing/AFOSR Mach-6 Quiet Tunnel at Purdue University, namely, a freestream Mach number of $M_\infty = 6$, unit Reynolds number $Re = 12.13\times10^6$ per meter, freestream static pressure $P_\infty = 702.62$ Pa, and a freestream temperature corresponding to $T_\infty = 51.92$ K. The temperature of the model surface, T_w, is equal to 300 K.

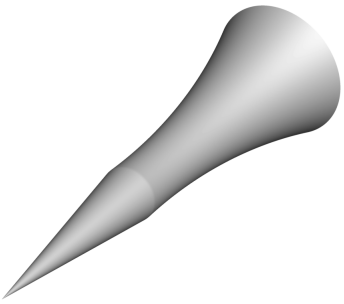

Figure 1. Schematic of straight-concave cone.

The computations of base flow for the secondary instability of Görtler vortices are carried out in two stages. The unperturbed boundary layer flow over the straight/concave body in the absence of any Görtler vortices are first computed via two different computer codes with different orders of accuracy and with different grid resolutions, to ensure adequate accuracy of the baseline flow field. First, we used a second order Navier-Stokes code, VULCAN, in conjunction with several grid resolutions to obtain a converged and shock-adapted solution for the entire cone. Then a subset of the computational domain was isolated for computations based on a seventh order DNS code, with the inflow location at 0.1 meters from the cone tip and extending in the wall-normal direction from the cone surface to just below the shock wave. Descriptions of these computational codes can be found in ref. [26]. The inflow and far-field boundary conditions for the DNS computation are based on the VULCAN solution. Figure 2 (a) shows a comparison between the VULCAN and DNS predictions for the wall pressure and wall heat flux along the cone surface obtained at different grid resolutions. The denser grid in DNS has twice the number of grid points in each spatial direction in comparison with the coarser grid. The wall heat flux is a sensitive metric for the accuracy of the basic state and its comparison as shown in Figure 2 (b) is a strong indication that the solution is grid converged.

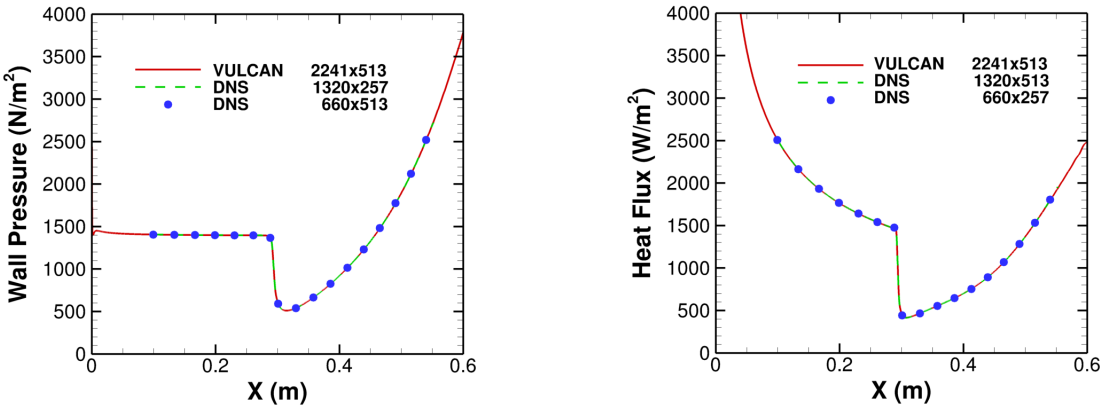

(a) Surface pessure distribution. **(b) Surface heat flux distribution.**

Figure 2. Comparison of surface pressure and heat flux distributions on different grids and/or via different numerical schemes.

The boundary layer profiles of the streamwise velocity and the temperature are plotted in Figures 3(a) and 3(b), respectively, for the same three cases as those shown in Figure 2. Profiles are plotted for five selected streamwise locations along the cone body. No difference can be discerned among the various solutions. Two of the velocity profiles at $X = 0.1$ *m* and 0.2 *m* on the forebody of the cone look like typical similarity profiles that one would expect to find in the boundary layer over a straight cone. The velocity profile at $X = 0.3$ *m* in the neighborhood of the junction between the forebody and the aft section begins to deviate from the similarity profiles, and the profiles at $X = 0.4$ *m* and 0.5 *m* even become inflectional as a result of the strong adverse pressure gradient over the concave portion of the

cone model (see Figure 2). All five temperature profiles shown in figure 3 (b) have a positive temperature gradient at the wall, indicating that the heat is transferred into the cone body.

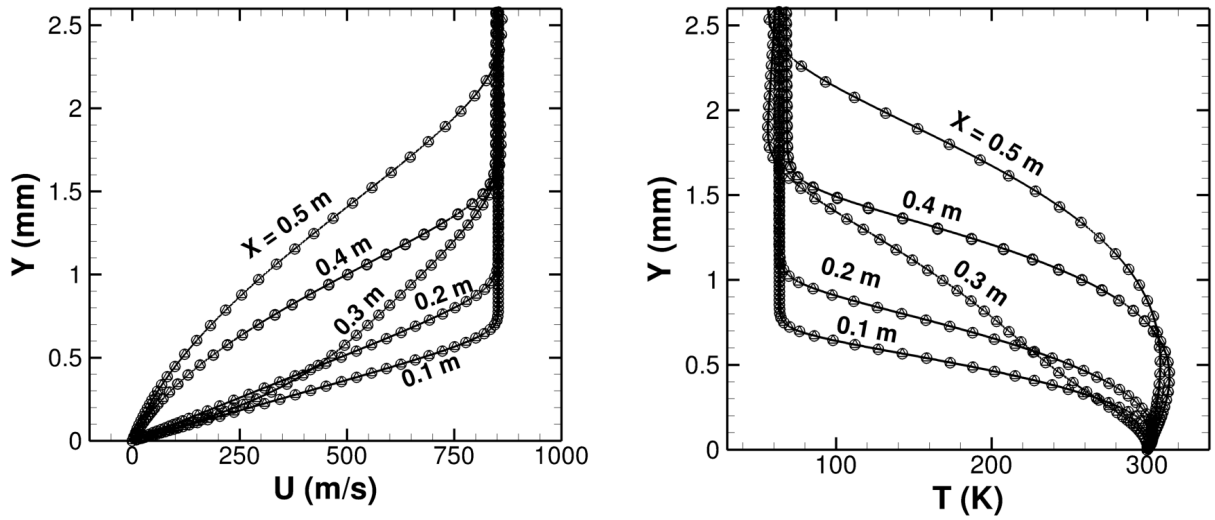

(a) Streamiwse velocity profiles. **(b) Temperature profiles.**

Figure 3. Velocity and temperature profiles at selected streamwise locations. Lines: VUCAN, 2241×513; triangles: DNS 1320×513; circles: DNS, 660×257.

The distribution of Görtler number, G, along the length of the cone is shown in Figure 4(a). The Görtler number equals approximately 6 near the start of the concave portion of the cone, reaches a maximum value of 10.2 at $X = 0.38$ m and decreases to just below 8 at the effective end of the cone. The boundary-layer edge Mach number plotted in Fig 4(b) is seen to be approximately uniform over the forebody of the cone. As the flow expands in the neighborhood of the maximum cone radius, the boundary-layer edge Mach number increases from slightly under 5.5 to a peak value of approximately 6.2, before it decreases again due to the compression over the concave portion of the cone. The axial variation in boundary-layer edge velocity from Figure 4(c) is similar to that of the edge Mach number. The axial variations in the boundary layer thickness as well as the displacement and momentum thicknesses are shown in figure 4(d). Each of those plots indicates a rapid thickening of the boundary layer above the concave portion as a result of the adverse pressure gradient in that region (see Fig 2(a)).

The next step in setting up the base flow for the secondary instability analysis at the flow condition of interest is to introduce the Görtler instability into the boundary layer. To select a representative wavenumber for the Görtler instability, linear N-factors for Görtler amplification are first computed for a range of azimuthal wavenumbers. The results are shown in Figure 5. In the upstream region, Görtler vortices with lower azimuthal wavenumbers have higher growth rates as seen in Fig. 5(a). As downstream locations are approached, the peak-growth wavenumber increases. The cumulative growth as represented by the wavenumber spectra of N-factors is shown in Fig. 5 (b) for a set of selected axial stations. Görtler vortices with an azimuthal wavenumber of 135 are predicted to have the highest amplification factor over the effective length of the cone. However, the N-factor spectrum at $X = 0.55$ m is relatively flat, indicating that Görtler vortices can experience strong growth across a broad range of wavenumbers.

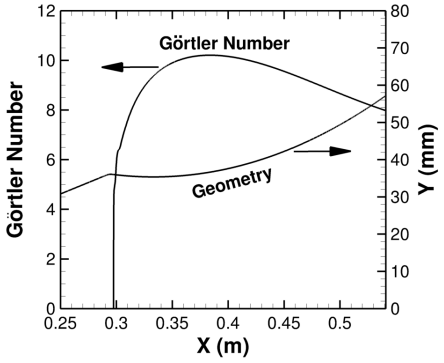

(a) Axial variation in Görtler number.

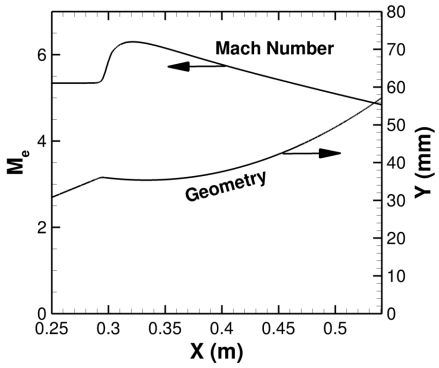

(b) Axial variation in boundary-layer edge Mach number.

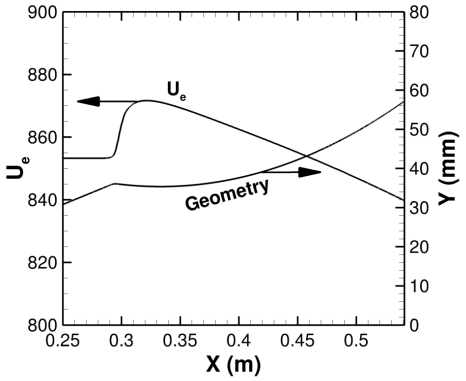

(c) Axial variation in boundary-layer edge velocity

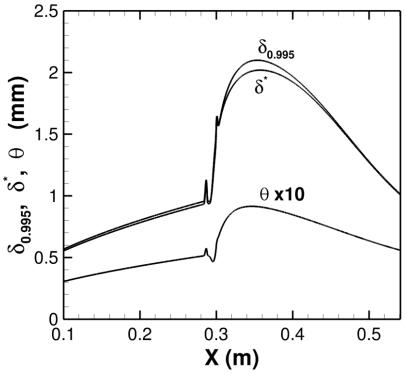

(d) Axial variation in boundary-layer thicknesses

Figure 4. Macroscopic properties of boundary layer.

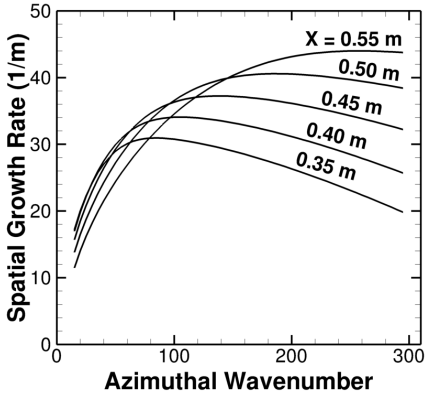

(a) N-factor evolution with streamwise distance. Each curve represents the spatial growth rate as a function of the azimuthal wavenumber for X values ranging from 0.35m to 0.55m in increments of 0.05m

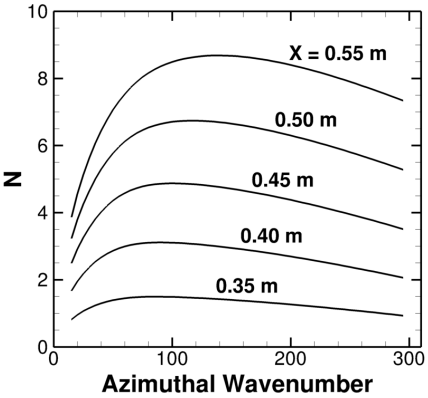

(b) N-factor spectrum at selected *X*-locations.

Figure 5 N-factors of linear Görtler instability.

For the analysis of secondary instability, we chose an azimuthal wavenumber of 100 similar to the prior work by Li et al. [26]. Since the array of oblique pairs of vortex generators from that paper may be difficult to fabricate with sufficient accuracy during an experiment, we employ an azimuthal array of elliptic planform protuberances in the present work. Specifically, 100 evenly spaced roughness elements in the form of protuberances with an elliptic planform are placed around the circumference of the cone. The axial location of the roughness array is chosen to be somewhat upstream of the junction between the fore and the aft bodies in an attempt to characterize the amplification of Görtler vortices over the entire downstream region with a concave curvature. The protuberance height, which is measured relative to an arbitrarily selected reference height of 0.005 *mm* (which corresponds to approximately 0.5% of the local boundary-layer thickness in the absence of the roughness), is varied to cover a range of initial (or, equivalently, the maximum) amplitude of the resulting Görtler vortices. A brief description of the numerical schemes used in the DNS code used for these computations can be found in ref. [24]. For the present configuration, a grid of 771×128×171 in the streamwise, azimuthal, and wall-normal directions is used. A grid convergence test is also carried out to establish that this grid resolution is sufficient in resolving the Görtler structures relevant to the present problem, using a denser grid of size 1028×192×257. For bump heights with $h/h_{ref} > 2.54$, the Görtler vortex amplitudes reach saturation ahead of the downstream computational boundary, after which the amplitudes no longer continue to grow exponentially and settle to values that amount to a maximum velocity amplitude that equals approximately 45% of the freestream velocity (Figure 6(a)). The amplitude evolution curves normalized by their respective values at $X = 0.32$ *m* are shown in Figure 6(b). Between $X = 0.30$ *m* and 0.38 *m*, the normalized amplitude evolution for all roughness configurations approximately collapse to a single curve. This is an indication that nonlinear effects in this region are small and that the Görtler amplification is close to linear, even for the case with the largest bump height (i.e., $h/h_{ref} = 10.0$). The amplitude curve corresponding to the largest bump height begins to peel off from the remaining curves just upstream of $X = 0.4$ *m*, followed by curves representing successively decreasing roughness heights that peel off at increasingly farther downstream locations, indicating the delayed onset of saturation in those cases. The normalized amplitude evolution for the two smallest bump heights is nearly the same throughout the entire computational domain, indicating that the Görtler instability continues to amplify exponentially until the outflow boundary and never reaches saturation in those two cases.

The distortion of the boundary layer flow due to the presence of finite amplitude Görtler vortices is examined next. Figure 7 shows the streamwise velocity contours in a crossplane at a streamwise location of $X = 0.48$ *m*, which is near the end of the effective computational domain for the four roughness heights. For the smallest height of $h/h_{ref} = 0.64$, the flow field is only slightly perturbed with the velocity contours displaying a barely discernable bulge. For a roughness height at $h/h_{ref} = 2,23$, the bell-shaped structure is formed. For a bump height at $h/h_{ref} = 4$, a "necking" takes place near the wall, resulting in velocity contours with a prominent mushroom structure. Finally, for the largest roughness height of $h/h_{ref} = 10$, strong mushroom "stems" become clearly visible. The roughness element heights of $h/h_{ref} = 4$ and $h/h_{ref} = 10$, respectively, correspond to approximately 2% and 5% of the local boundary layer thickness, indicating that relatively significant roughness heights are required to produce the mushroom structure. Thus, an equivalent forcing is unlikely to be produced via naturally occurring surface roughness on a wind tunnel model with a typical level of surface quality.

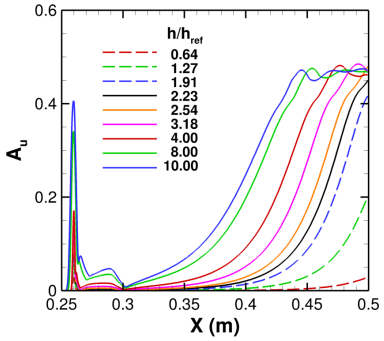

(a) Vortex amplitudes as fractions of freestream velocity.

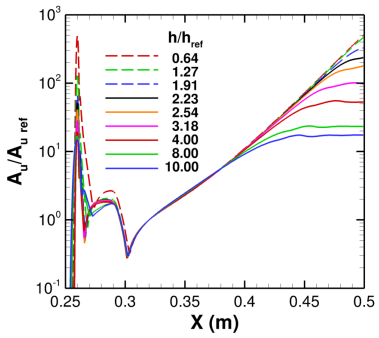

(b) Vortex amplitudes normalized by the respective values at $X = 0.32$ *m*.

Figure 6. Amplitude evolution of Görtler vortices generated by roughness array of various heights.

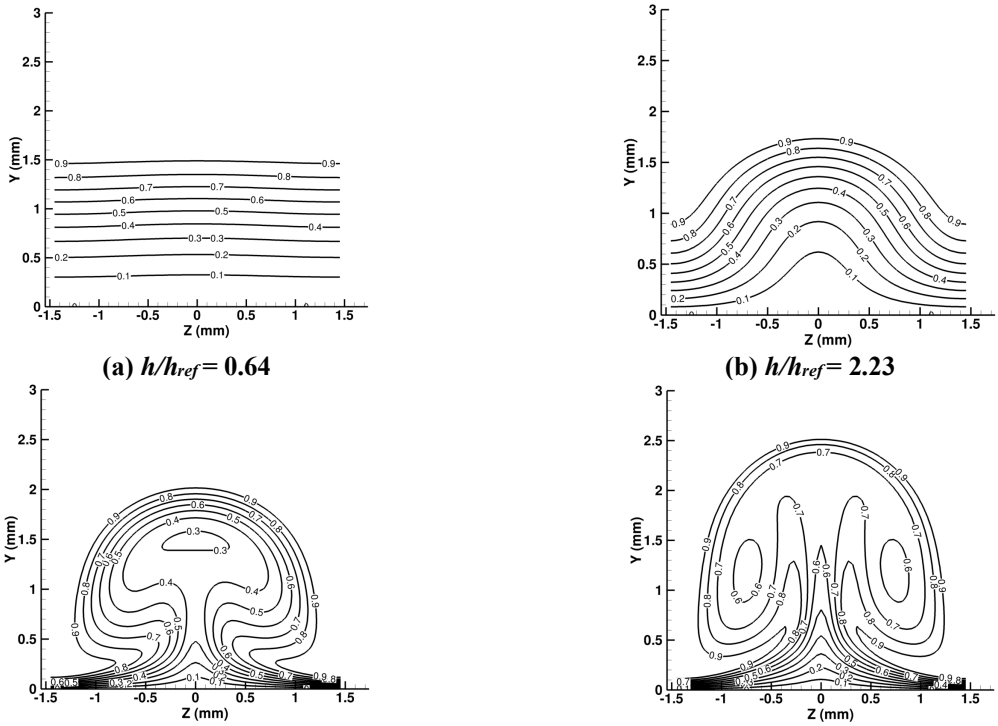

(a) h/h_{ref} = 0.64 **(b) h/h_{ref} = 2.23**

(c) h/h_{ref} = 4 **(d) h/h_{ref} = 10**

Figure 7. Streamwise velocity contours at X = 0.48 m for selected bump heights.

Figure 8 shows the downstream evolution of Görtler vortices at several streamwise locations with a fixed axial interval of ΔX = 0.025 m for the case of h/h_{ref} = 10. The bulging of the streamwise velocity contours near the azimuthal symmetry plane in the middle is already obvious at X = 0.325 m. By X = 0.4 m, the bell-shaped contours seen during the previous studies [24-26] are formed. Farther downstream, the lower part of the "bell" close to the wall begins to narrow significantly, accompanied by a rapid thinning of the boundary layer on either side of the "bell". Still farther downstream, a necking process occurs so that the near-wall fluid on either side of the "bell" is entrained toward the center by the strong Görtler vortices, leading to the formation of a mushroom structure with a strong shear layer around the mushroom cap, as is often observed at lower Mach numbers [21, 25]. At the final two stations, figures 8(g) and 8(h) show that the entrained fluid is brought upwards on either side of the mushroom stem to form internal, nearly vertical shear layers associated with a higher shear than that around the mushroom cap. Figure 8(h) also shows the in-plane streamlines over the right half of the mushroom structure, which is similar to those obtained by Chen et al. [31].

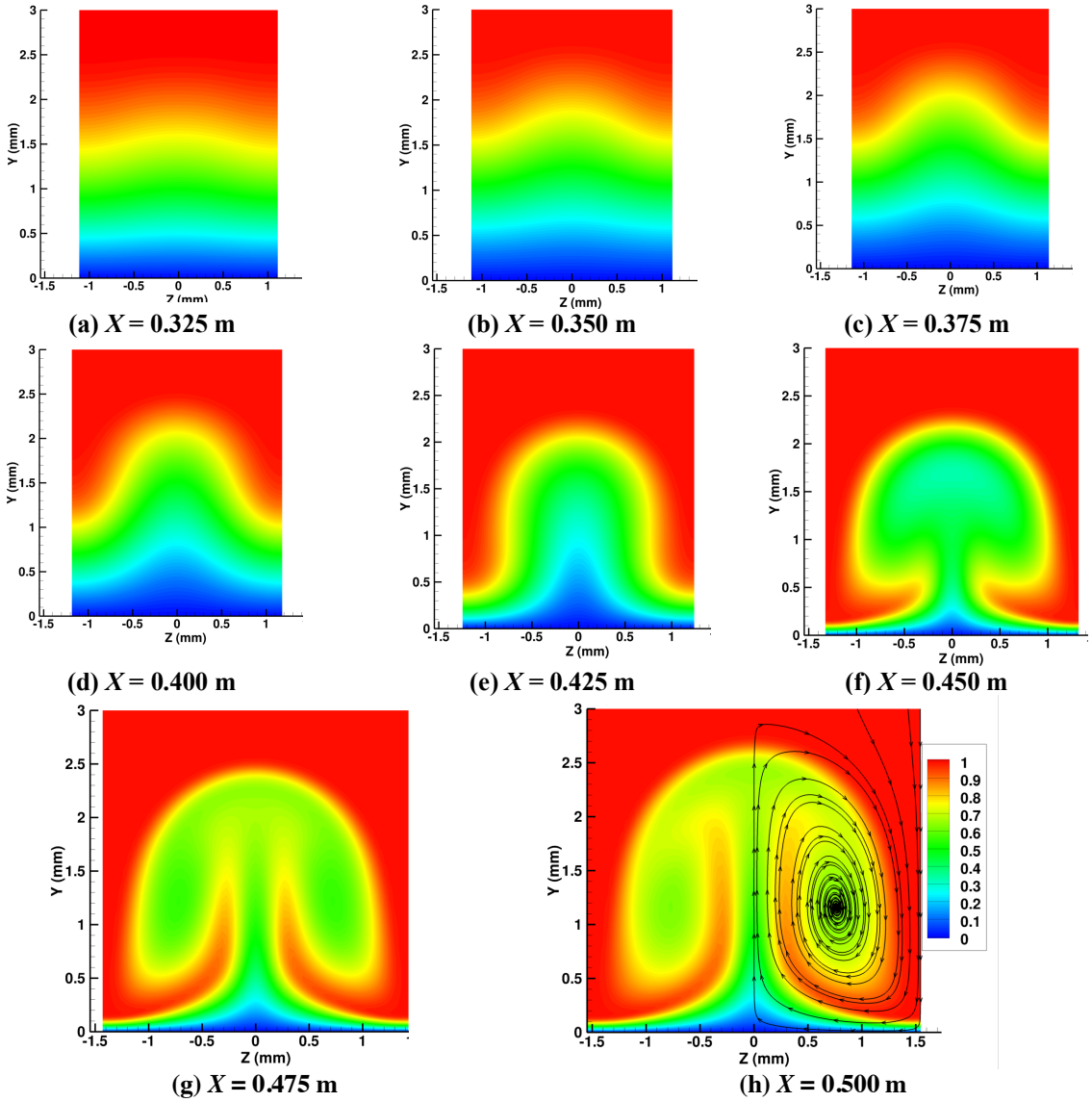

Figure 8. Evolution of Görtler vortices generated by azimuthally periodic roughness distribution with $h/h_{ref} = 10$. Streamwise velocity contours are shown.

III. Secondary Instability

Secondary instability computations were carried out for selected roughness heights by solving a planar eigenvalue problem at each axial location from the DNS computation. The results presented here correspond to the fundamental modes, i.e., to modes with an azimuthal wavelength that is identical to the fundamental wavelength of the underlying roughness configuration. Subharmonic modes are also present with comparable growth rates, but we will defer their presentation to a future paper. Modes with both symmetric and antisymmetric boundary conditions for the fluctuations are considered for $h/h_{ref} = 2.23$, 4, and 10 at $X = 0.498$ m. For a moderate roughness height of $h/h_{ref} = 2.23$, the growth rate spectrum is relatively simple, with three highly unstable symmetric modes and two antisymmetric modes as shown

in Figures 9(a) and 9(b), respectively. As the roughness height increases to $h/h_{ref} = 4$, the number of unstable modes with comparable amplification rates also increases, especially in the case of the antisymmetric modes, yielding a total of four symmetric modes and five antisymmetric modes as depicted in figures 9(c) and 9(d), respectively. Because of the strong mushroom structures at the largest roughness height of $h/h_{ref} = 10$, the spectrum of unstable secondary modes includes five symmetric and five antisymmetric modes with peak growth rates that exceed an arbitrarily selected threshold of 50 m^{-1} (Figs. 9(e) and 9(f), respectively). Figure 9(e) shows the growth rate spectrum at $X = 0.498$ *m* for the five symmetric modes and Figure 9(f) shows similar spectra for the leading five antisymmetric modes for $h/h_{ref} = 10$.

Given the azimuthal symmetry characteristics of the Görtler vortex pair, the base flow used in the secondary instability computations consists of only half the azimuthal domain from the full wavelength domains shown in Figure 8. This choice of the computational domain reduces the cost of the secondary instability computations. Grid convergence tests were performed to ensure the numerical accuracy of the results at $X = 0.498$ *m* for the $h/h_{ref} = 10$ case. This particular station is very close to the downstream end of the computational domain, and therefore, the Görtler vortex amplitude is close to its global peak, and hence, the secondary instability growth is also at its strongest within the entire domain of analysis. The growth rate spectra are computed using three different grids with spanwise and streamwise resolutions of 45×181, 45×241 and 65×181, respectively. The agreement among the predicted growth rates computed via the different grids is very good as seen in Figures 9(e) and 9(f), where the lines, triangles, and the circles represent the above three grid resolutions. The five symmetric modes of secondary instability are denoted as *S1* through *S5* (Figure 9 (e)) and the five leading antisymmetric modes are denoted as *A1* through *A5,* respectively, in Figure 9(f). The highest peak growth rate among the symmetric modes at $X = 0.498$ *m* corresponds to Mode *S1*, which corresponds to a modulated Mack mode as shown later in this paper. The peak growth rate of this mode is just below 200 m^{-1}, corresponding to a disturbance frequency of approximately 400 *kHz*. Modes *S2* through *S4* are genuine secondary instability modes that would not be unstable in the absence of Görtler vortices of sufficient amplitude. The nature of Mode *S5* is most likely a modulated Mack mode. For the antisymmetric modes at the same streamwise location, a somewhat higher peak growth rate of approximately 250 m^{-1} is attained by Mode *A1*. Both symmetric and antisymmetric modes of secondary instability extend up to a frequency of approximately 900 *kHz*, which corresponds to a substantially larger frequency bandwidth than that of the second mode (i.e., Mack mode) instability in the unperturbed boundary layer without any Görtler vortices.

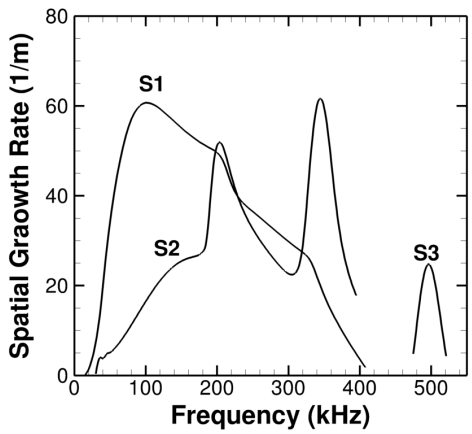

(a) h/h_{ref} = 2.23, symmetric

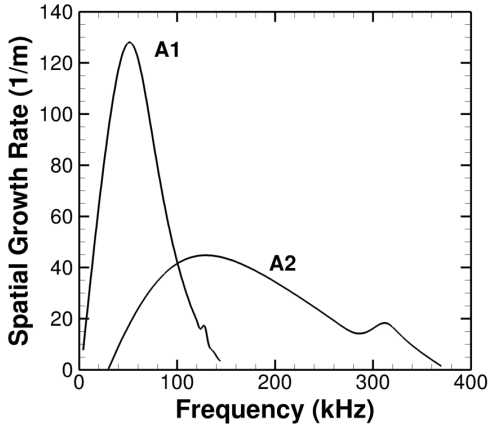

(b) h/h_{ref} = 2.23, antisymmetric.

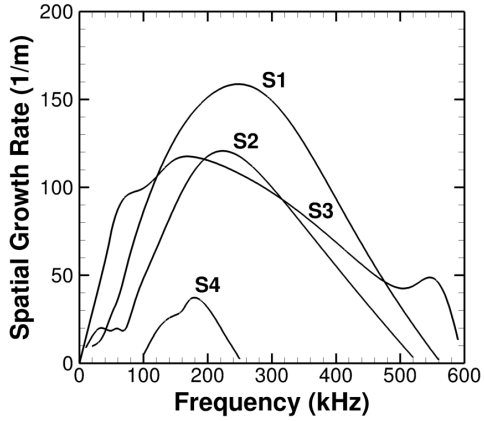

(c) h/h_{ref} = 4, symmetric.

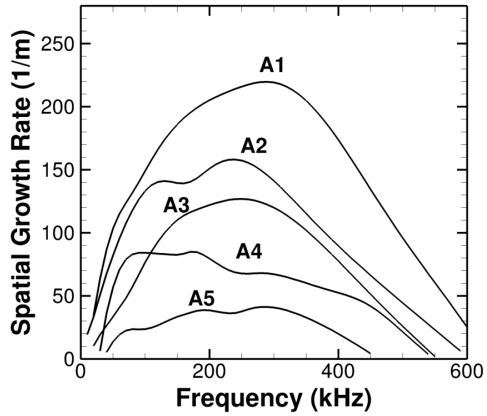

(d) h/h_{ref} = 4, antisymmetric.

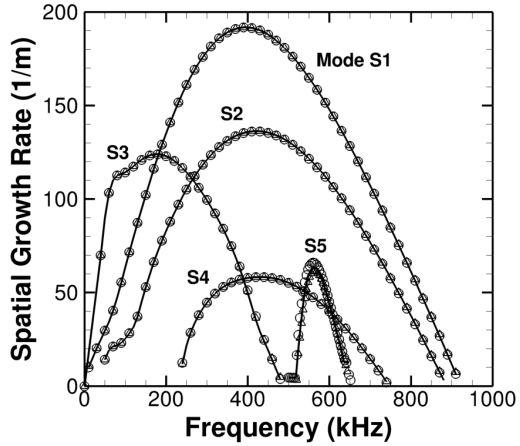

(e) h/h_{ref} = 10, symmetric.

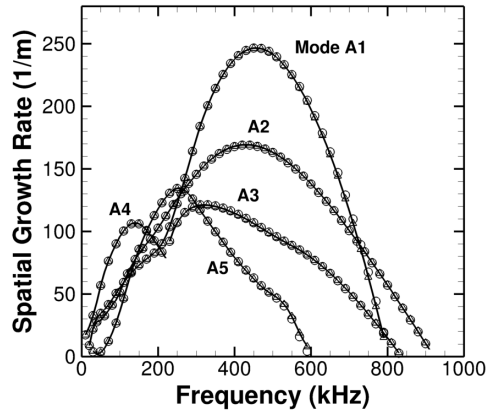

(f) h/h_{ref} = 10, antisymmetric.

Figure 9. Secondary instability growth rates for selected bump heights.

The eigenfunctions for the streamwise velocity perturbation associated with the five symmetric modes of secondary instability are shown in Figure 10. The colored flood contours represent the RMS fluctuation in the streamwise perturbation velocity, normalized to a peak value of unity across the cross section of the vortex. The white lines indicate the mushroom structure associated with the streamwise velocity contours of the stationary base flow with finite amplitude Görtler vortices. Peak fluctuations associated with Mode *S1* are observed to lie along the top of the

mushroom structure, whereas the peak fluctuations induced by the Mode *S2* wrap around the edge of the mushroom cap, on either side of the symmetry plane. Modes *S3* and *S5* are concentrated in the strong vertical shear layer in the vicinity of the stem region underneath the mushroom cap. Finally, mode *S4* has its peak amplitude close to the wall on either side of the mushroom.

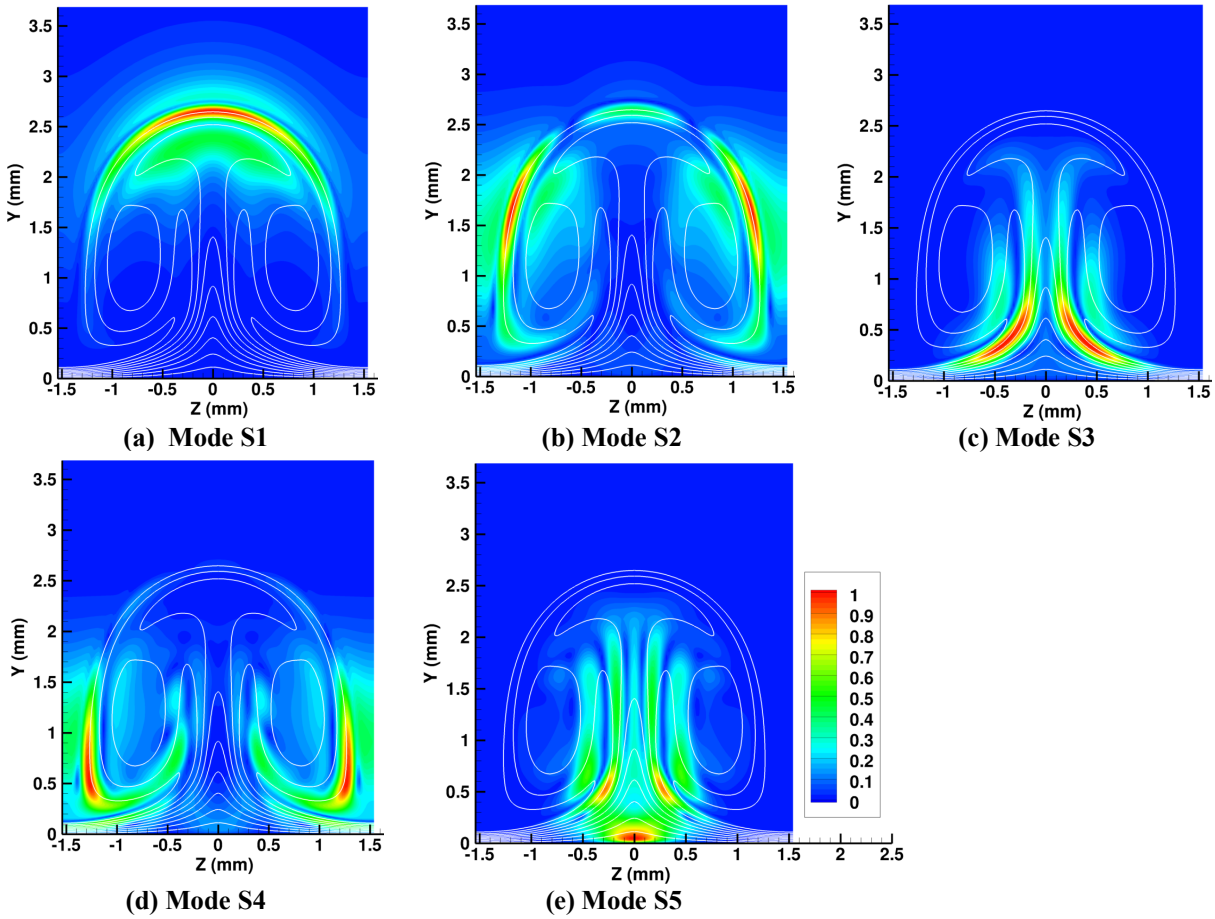

Figure 10. Streamwise perturbation velocity eigenfunctions of symmetric modes.

The streamwise velocity eigenfunctions of the leading eight antisymmetric modes (including the 5 modes shown in Figure 9 (f) and three additional modes with relatively small growth rates) are shown in Figure 11. The apparent symmetry of the mode shapes is because the contours corresponds to a positive semidefinite metric corresponding to the RMS fluctuation in streamwise velocity. The perturbations in the streamwise velocity on either side of the azimuthal symmetry plane of the basic state are actually 180 degrees out of phase with each other. The amplitudes of Modes A2, A3 and A8 are concentrated near the sides of the mushroom, while the remaining five modes are stem modes that were previously unknown for Görtler instability at hypersonic speeds.

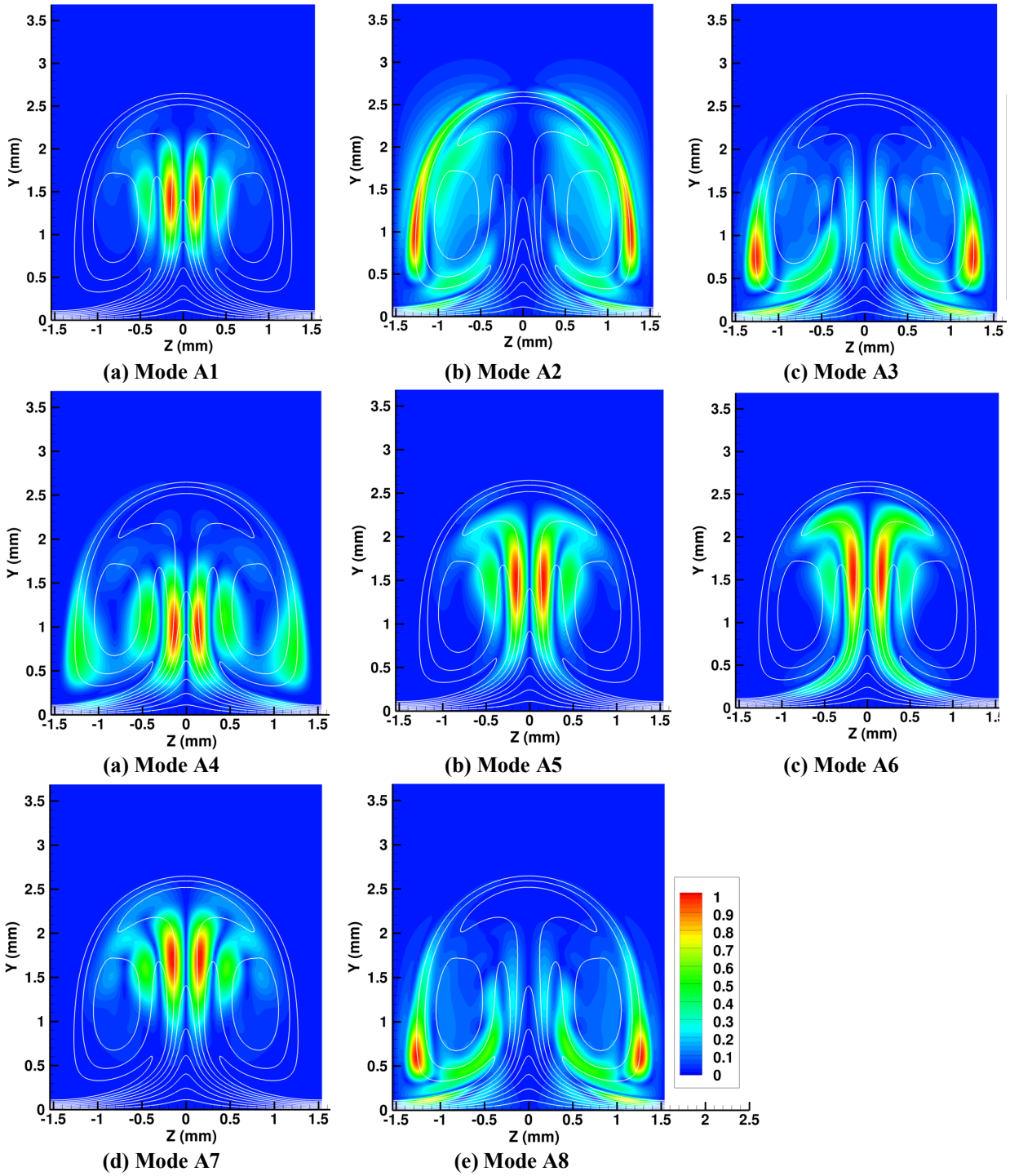

Figure11. Streamwise perturbation velocity eigenfunctions of antisymmetric modes.

In addition to inducing strong fluctuations in the streamwise velocity component, the secondary instability of Görtler vortices is also characterized by large perturbations in the flow temperature, and the highest temperature fluctuations are concentrated in similar cross-plane locations as the peak fluctuations in the streamwise velocity. For that reason, the mode shapes for the temperature fluctuations are not be shown in this paper.

The secondary instability characteristics discussed above pertains to the single streamwise station of $X = 0.498\ m$. However, a mode that is locally most unstable may not have the highest cumulative growth over the axial region of interest. To identify the modes with the highest amplification ratios over the region of instability, Figure 12 shows the N-factor curves for both the symmetric and antisymmetric modes. For the largest roughness height of $h/h_{ref} = 10$ (Figures 12(a) and 12(b), respectively), the most amplified symmetric mode is Mode *S1*, which attains an N-factor of just over 8 for a disturbance frequency of 130 *kHz*. This mode becomes unstable much earlier than the remaining symmetric modes, where the Görtler vortex amplitude is deemed to be too small to support any genuine secondary instability. Therefore, one expects mode *S1* to be an azimuthally modulated form of the axisymmetric Mack mode, similar to the mode that exists for a small Görtler vortex amplitude as reported by Li et al. [26]. Further evidence that mode *S1* is a modulated Mack mode is given in Figure 13, in which the growth rate spectrum of the Mack mode and the *S1* mode are plotted together. The good agreement leaves little doubt that the unstable mode *S1* originates from the Mack mode instability. As the stationary Görtler vortex becomes stronger in amplitude, it enables this modulated Mack mode to sustain its growth over a significantly larger axial region than the pure Mack mode in the unperturbed boundary layer without any Görtler vortices. Indeed, the higher slopes of the N-factor curves in the aft part of the domain shown in Fig. 12 indicate that the peak growth rates of mode *S1* are also higher than the peak growth rates of the Mack mode instability. The higher values of the peak growth rates, combined with a longer region of instability, enable the mode *S1* perturbations to achieve larger N-factors in comparison with the Mack modes in the unperturbed boundary layer. These findings highlight the destabilizing influence of finite amplitude Görtler vortices on the Mack mode instability, analogous to the earlier computations by Li et al.[29] and DNS results by Choudhari et al. [30] in the context of secondary instability of stationary crossflow vortices on a yawed cone in a hypersonic free stream.

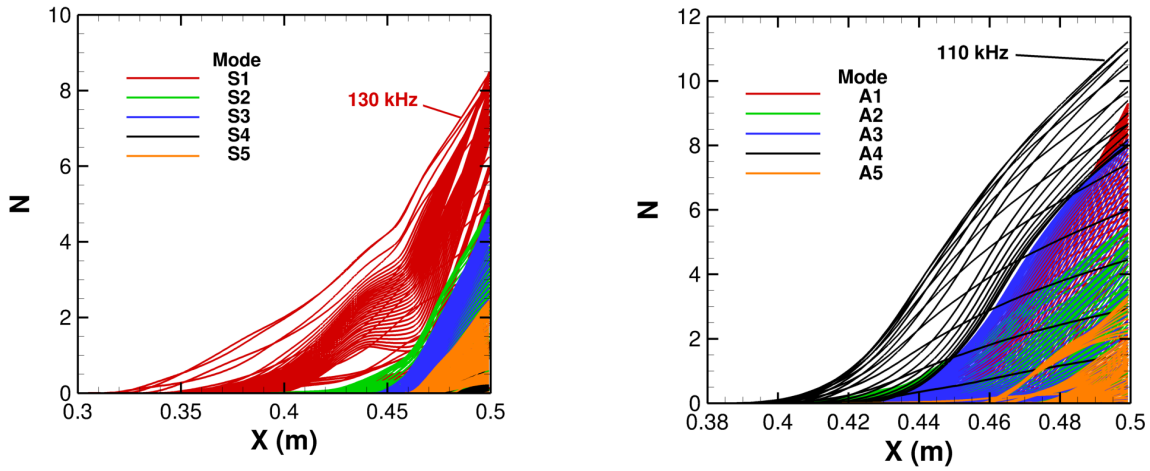

(a) Symmetric modes. **(b) Antisymmetric modes.**

Figure 12. N-factors of fundamental secondary instability modes for $h/h_{ref} = 10$.

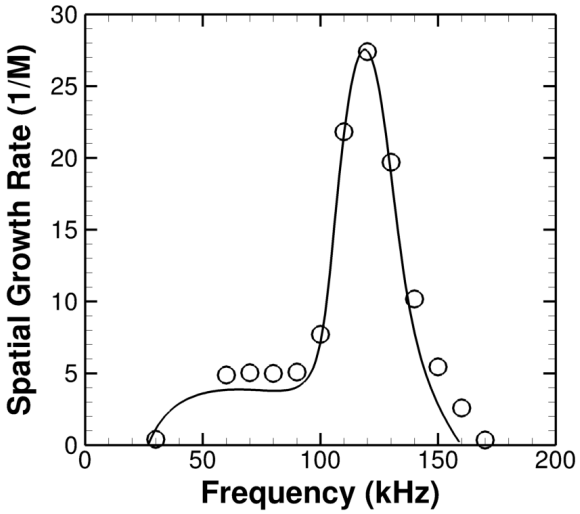

Figure 13. Comparison of Mack mode (line) and *S1* mode (circles) growth rate spectra at X = 0.35 m for h/h_{ref} = 10.

IV. Summary and Concluding Remarks

It is shown that the mushroom-shaped structures do exist for sufficiently large initial amplitudes, supporting the observations by Whang and Zhong [19] and computations of Chen et al. [31]. For low initial amplitudes, the peak amplitude of the Görtler vortices over the length of the cone remains sufficiently small so as to induce only sinusoidal modulation of the boundary layer flow along the azimuthal coordinate. For moderate initial amplitudes, the peak amplitude becomes large enough to give rise to bell-shaped structures found by Li et al. [26] and Ren and Fu [25]. The mushroom structures are observed when the initial amplitude is sufficiently large, which gives rise to a prominent quasisaturation behavior that is analogous to that observed in lower Mach number flows. In that respect, the amplitude evolution of Görtler vortices in hypersonic boundary layers as well as the resulting structures in the nonlinear regime are quite analogous to those in lower Mach number flows excepting an increased significance of the thermal streaks. Computations also revealed that the dominant modes of secondary instability in these mushroom-shaped structures correspond to an antisymmetic (i.e., sinuous) "stem" mode that concentrates within the strong, nearly wall-normal internal shear layers surrounding the stem regions underneath the caps of the mushroom structures. Additionally, there exist a multitude of other significantly unstable secondary instability modes of both symmetric and antisymmetric types. Analogous to the secondary instability of crossflow vortices in hypersonic flows, secondary instability modes originating from the Mack mode instability play an important role during the nonlinear breakdown process. In a follow-on effort to this work, we have performed additional DNS to examine the nonlinear aspects of the receptivity process for the primary Görtler instability and examined the nonparallel effects on the evolution of the secondary instability characteristics by using plane-marching PSE. The results of these computations will be reported in a separate paper.

Acknowledgments

The work of the NASA authors was performed as part of the Hypersonic Technology Project and the Revolutionary Computational Aerosciences discipline under the Transformational Tools and Technologies project of the NASA Transformative Aeronautics Concepts Program. Computational resources for this research were provided by the NASA High-End Computing (HEC) Program through the NASA Advanced Supercomputing (NAS) Division at Ames Research Center.

References

[1] Görtler, H., "On the Three-Dimensional Instability of Laminar Boundary Layers on Concave Walls," NACA TM 1375, 1954; translated from "Über eine Dreidimensionale Instabilität Laminarer Grenzschichten an Konkaven Wänden. Des. D. Wiss. Göttingen, Nachr 1940, 1940, 1 (2).

[2] Hall, P., "Taylor-Görtler Vortices in Fully Developed or Boundary-Layer Flows: Linear Theory," *J. Fluid Mech.*, Vol. 124, 1982, pp. 475–494.

[3] Hall, P., "The Linear Development of Görtler Vortices in Growing Boundary Layers," *J. Fluid Mech.*, Vol. 130, 1983, pp. 41–58

[4] Hall, P., "Görtler Vortices in Growing Boundary-Layers: The Leading-Edge Receptivity Problem, Linear Growth and the Nonlinear Breakdown Stage," *Mathematika*, Vol. 37(2), 1990, pp. 151–189.

[5] El-hady, N. M. and Verma A. K., "Growth of Görtler Vortices in Compressible Boundary Layers along Curved Surfaces," AIAA Paper 1981-1278, 1981.

[6] Hall, P. and Malik, M., "The Growth of Görtler Vortices in Compressible Boundary Layers," *J. Eng. Math.*, Vol. 23, 1989, pp. 239–251.

[7] Hall, P. and Fu, Y., "On the Görtler Vortex Instability Mechanism at Hypersonic Speeds," *Theoretical and Computational Fluid Dyn.*, Vol. 1(3), 1989, pp. 125–134.

[8] Fu, Y. and Hall, P., "Effects of Görtler Vortices, Wall Cooling, and Gas Dissociation on the Rayleigh Instability in a Hypersonic Boundary Layer," *J. Fluid Mech.*, Vol. 247, 1993, pp. 503–525.

[9] Fu, Y., Hall, P., and Blackaby, N., "On the Görtler Instability in Hypersonic Flows: Sutherland Law Fluids and Real Gas Effects," *Phil. Trans. Royal Soc. A*, Volume 342, issue 1665, 1993, pp. 325–377

[10] Fu, Y. and Hall, P., "Crossflow Effects on the Growth Rate of Inviscid Görtler Vortices in a Hypersonic Boundary Layer," *J. Fluid Mech.*, Vol. 276, 1994, pp. 343–367.

[11] Chen, F.-J., Wilkinson, S. P., and Beckwith, I. E., "Görtler Instability and Hypersonic Quiet Nozzle Design," *J. Spacecraft and Rockets*, Vol. 30 (2), 1993, pp. 170–175.

[12] Dando, A. H. and Seddougui, S. O., "The Compressible Görtler Problem in Two-Dimensional Boundary Layers," *IMA J. Appl. Math.*, Vol. 51(1), 1993, pp. 27–67.

[13] Spall, R. E. and Malik, M. R., "Goertler Vortices in Supersonic and Hypersonic Boundary Layers," *Physics of Fluids A*, Vol. 1, 1994, pp. 1822–1835.

[14] Kobayashi, R. and Kohama, Y., "Taylor-Görtler Instability of Compressible Boundary Layers," *AIAA Journal*, Vol. 15, No. 12, December 1977.

[15] Schneider, S. P., "Design of a Mach-6 Quiet-Flow Wind-Tunnel Nozzle Using the e**n Method for Transition Estimation," AIAA Paper 1998-0547, 1998.

[16] Whang, C. W. and Zhong, X. L., "Direct Numerical Simulation of Görtler Instability in Hypersonic Boundary Layers," AIAA Paper 1999-291, 1999.

[17] Whang, C. W. and Zhong, X. L., "Nonlinear Interaction of Görtler and Second Modes in Hypersonic Boundary Layers," AIAA Paper 2000-536, 2000.

[18] Whang, C. W. and Zhong, X. L., "Receptivity of Görtler Vortices in Hypersonic Boundary Layers," AIAA Paper 2002-151, 2002.

[19] Whang, C. W. and Zhong, X. L., "Leading Edge Receptivity of Görtler Vortices in a Mach 15 Flow over a Blunt Wedge," AIAA Paper 2003-0790, 2003.

[20] Hall, P. and Horseman, N. J., "The Linear Inviscid Secondary Instability of Longitudinal Vortex Structures in Boundary Layers," *J. Fluid Mech.*, 232, pp. 357-375, 1991.

[21] Li, F., and Malik, M. R., "Fundamental and Subharmonic Secondary Instabilities of Görtler Vortices," *J. Fluid Mech.*, Vol. 297, pp. 77-100, 1995.

[22] Jiang, L., Choudhari, M., Chang, C.-L., and Liu, C., "Direct Numerical Simulations of Crossflow Disturbances in Supersonic Boundary Layers," AIAA Paper 2004-589, 2004.

[23] Choudhari, M., Li, F., and Edwards, J., "Stability Analysis of Roughness Array Wake in a High-Speed Boundary Layer," AIAA Paper 2009-0170, 2009.

[24] Li, F., Choudhari, M. M., Chang, C.-L., Wu, M., and Greene, P. T., "Development and Breakdown of Görtler Vortices in High Speed Boundary Layers," AIAA Paper 2010-705, 2010.

[25] Ren, J. and Fu S., "Secondary Instabilities of Görtler Vortices in High-Speed Boundary Layers," *J. Fluid Mech.*, Vol. 781, 2015, pp. 388–421.

[26] Li, F., Choudhari, M. M., Paredes, Schneider, S. P. and Portoni, P., "Görtler Instability and Its Control via Surface Suction Over an Axisymmetric Cone at Mach 6,", AIAA paper 2018-3069.

[27] Saric, W. S., "Görtler Vortices," *Annu. Rev, Fluid Mech*., Vol. 25, 1994, pp. 379-409.

[28] Schneider, S. P., "Development of Hypersonic Quiet Tunnels," *Journal of Spacecraft and Rockets*, Vol. 45, No. 4, July-August 2008, pp 641-664.

[29] Li, F., Choudhari, M., Paredes, P., and Duan, L., "High-Frequency Instabilities of Stationary Crossflow Vortices in a Hypersonic Boundary Layer," *Phys. Rev. Fluids*, Vol. 1, 2016, 053603.

[30] Choudhari, M., Li, F., Paredes, P., and Duan, L., "Nonlinear Evolution and Breakdown of Azimuthally Compact Crossflow Vortex Pattern over a Yawed Cone," AIAA Paper 2018-1823, 2018.
[31] Chen, X., Huang, G. L., and Lee, C. B., "Hypersonic Boundary Layer Transition on a Concave Wall: Stationary Görlter vortices," *J. Fluid Mech.*, Vol. 865, 2019, pp. 1-40.